

Nanoscale

Accepted Manuscript

This article can be cited before page numbers have been issued, to do this please use: G. Bhattacharya, I. Lionadi, S. McMichael, M. Taverne, J. McLaughlin, P. Fernandez-Ibanez, C. Huang, Y. D. Ho and A. Farokh Payam, *Nanoscale*, 2025, DOI: 10.1039/D5NR03147H.



This is an Accepted Manuscript, which has been through the Royal Society of Chemistry peer review process and has been accepted for publication.

Accepted Manuscripts are published online shortly after acceptance, before technical editing, formatting and proof reading. Using this free service, authors can make their results available to the community, in citable form, before we publish the edited article. We will replace this Accepted Manuscript with the edited and formatted Advance Article as soon as it is available.

You can find more information about Accepted Manuscripts in the [Information for Authors](#).

Please note that technical editing may introduce minor changes to the text and/or graphics, which may alter content. The journal's standard [Terms & Conditions](#) and the [Ethical guidelines](#) still apply. In no event shall the Royal Society of Chemistry be held responsible for any errors or omissions in this Accepted Manuscript or any consequences arising from the use of any information it contains.

Two Dimensional-Material-Coated Microcantilevers for Enhanced Mass Sensing and Material Characterization

Gourav Bhattacharya¹⁺, Indrianita Lionadi¹⁺, Stuart McMichael¹, Mike P. C. Taverne^{2,3}, James McLaughlin¹, Pilar Fernandez-Ibanez¹, Chung-Che Huang^{4,*}, Ying-Lung Daniel Ho^{2,3,*}, Amir Farokh Payam^{1,*}

¹Nanotechnology and Integrated Bioengineering Centre, School of Engineering, Ulster University, Belfast, UK.

²Department of Mathematics, Physics & Electrical Engineering, Northumbria University, NE1 8ST Newcastle upon Tyne, UK.

³Department of Electrical and Electronic Engineering, University of Bristol, BS8 1UB Bristol, UK.

⁴Optoelectronics Research Centre, University of Southampton, SO17 1BJ Southampton, UK.

⁺equal contributions

cch@soton.ac.uk; daniel.ho@northumbria.ac.uk; a.farokh-payam@ulster.ac.uk

Abstract

The integration of 2D material coatings on microcantilevers marks a transformative advancement in nanomechanical sensing. As essential components of nanomechanical sensors, microcantilevers detect minute forces, such as molecular interactions, through frequency shift measurements, enabling ultra-sensitive detection with atomic-scale mass resolution. This work emphasizes the novelty of employing 2D-material coatings on microcantilevers, presenting an integrated approach that combines theoretical modeling, simulation, and experimentation. By utilizing 2D-material-coated microcantilevers, this study demonstrates the precise measurement of mass, Young's modulus and thickness of 2D material layers. The enhanced performance of these coated resonators is showcased in applications such as bacterial and uric acid mass sensing at varying concentrations, achieving superior frequency detection, responsivity, and accuracy.

This research not only advances nanoscale sensor design but also underscores the potential of 2D-material coatings in revolutionizing nanoelectromechanical sensors for materials characterization and mass spectrometry, paving the way for next-generation sensing technologies.

Introduction

Microcantilevers play a central role in imaging and sensing in both atomic force microscopy (AFM) and nanoelectromechanical sensors^{1–6}. Thanks to the progress in micro- and nanofabrication technologies, we can now create smaller cantilever-based nanomechanical resonators. These miniature structures are adept at detecting forces, masses, mechanical properties, and motion associated with molecular interactions and surface forces at the molecular/atomic levels^{7–11}.

For mass measurements, nanomechanical devices have undergone significant advancements, reaching a stage where they present a compelling opportunity to revolutionize mass spectrometry. Nanoelectromechanical systems (NEMS) resonators exhibit remarkable sensitivity or in other word responsivity to the added mass of adsorbed particles^{12–16}. This progress has resulted in significant



achievements, including the detection of the mass of individual proteins¹⁷, nanoparticles^{18,19} and large biomolecules^{20,21}. Moreover, there have been demonstrations of near-atomic-scale mass resolution^{22,23}.

However, when the mass and sizes of the adsorbent significantly differ from the mass and geometry of the cantilever, the accurate mass quantification is compromised. This is due to the microcantilever's sensitivity and the coupling between changes in its stiffness and mass. As a result, this could lead to mismatches in the detected masses potentially exceeding 50%⁹. Another finding of the research indicates that when microcantilevers are used in applications with adsorbed layers, the mechanical properties of these coated cantilevers can show substantial variations compared to their pristine counterparts^{7,19}. Previous studies have elucidated that variations in the spring constant of microcantilevers are attributed to alterations in stress on one side of the cantilever⁷. Nevertheless, in those experiments, the effect of the mass of the adsorbed layer was negligible due to the cantilever being considerably larger in mass compared to the adsorbed layer. While some studies have attempted to address the influence of the particle mass and spatial distribution on nanoscale sensors²⁴, the phenomenon of observed anomalous frequency shifts is still needed more studies²⁵. Furthermore, despite significant advancements in using microcantilevers as sensing tools, their characterization capability remains elusive.

Recent advances in the synthesis and preparation of 2D materials^{26,27} provide a significant opportunity to utilize them in microcantilever-based nanomechanical sensors and energy harvesters²⁸. These novel materials can be applied as a coating to the microcantilever, enhancing its ability to detect with high responsivity. For example, Molybdenum disulfide (MoS₂) has unique physical and mechanical properties such as high surface area, flexibility and stiffness²⁹, which can be adjusted by changing the number of layers or incorporating defects. This tunability allows for the customization of cantilever designs with desired mechanical characteristics for specific sensing applications. The surface of the MoS₂ can be easily functionalized²⁸ and also, they possess a tunable higher electron mobility²⁸. These properties make them a suitable candidate for an efficient sensing platform. This integration of 2D materials with microcantilevers allows for precise control over the cantilever's resonant frequency and significant improvements in the minimum detectable frequency and sensitivity of mass spectrometry, enabling applications in high-precision sensing.

In this work, we employ the concept of a digital twin to develop an integrated theoretical, simulation and experimental methodology. This method elucidates the effect of coating and layer adsorption mechanisms on the characteristics of nanomechanical resonators, explores the origin of observed anomalous frequency shifts, and quantifies the properties of the coated layers.

Experimentally, we introduce a technique to uniformly coat the microcantilever surface with large-scale MoS₂ through Van der Waals epitaxy. Subsequently, the theoretical model allows us to measure the mass and quantify Young's modulus, thickness, and layer count of the MoS₂ directly from the measured frequency and spring constant of the coated microcantilever. We used two methods to determine the mass, thickness, and Young's modulus of the deposited MoS₂. In Method 1, Raman spectroscopy and



HRTEM were employed to determine the number of MoS₂ layers. Using the cantilever's geometry, we calculated the MoS₂ mass, which, combined with frequency measurements, allowed us to compute the cantilever's spring constant. Applying composite beam theory, we then extracted the Young's modulus of the MoS₂ layer. In Method 2, we measured the cantilever's frequency and spring constant before and after MoS₂ deposition. Using an updated cantilever mass spectrometry model, we calculated the MoS₂ mass, and from the mass, frequency shift, and spring constant, we derived its thickness and Young's modulus. We then utilize the MoS₂-coated microcantilever to measure the mass of *Escherichia coli* (*E. coli*) bacteria, demonstrating a significant improvement in its minimum frequency detection, which is approximately 4-times superior to that of a pristine cantilever. This results in higher sensitivity and accuracy in mass spectrometry. Furthermore, to show the trends in accurately measuring the mass of adsorbent using the modified MoS₂ microcantilever and also the importance of considering the stiffness change in mass measurements, we used our modified microcantilevers to measure the mass of adsorbed uric acid with different concentrations on the surface of microcantilevers. Our results clearly show the higher responsivity and accuracy of our modified MoS₂ microcantilever in detecting the mass of added uric acid with different concentrations.

This approach is a breakthrough in the characterization of 2D materials. It could also pave the way for the design and fabrication of a new generation of microcantilevers that benefit from the unique properties of 2D materials for use in sensing applications.

Methodology

The schematic of our integrated methodology is given in Fig. 1. For our presented analysis, the cantilever geometry is approximated as an ideal rectangular shape with a coated MoS₂ as a 2D material.



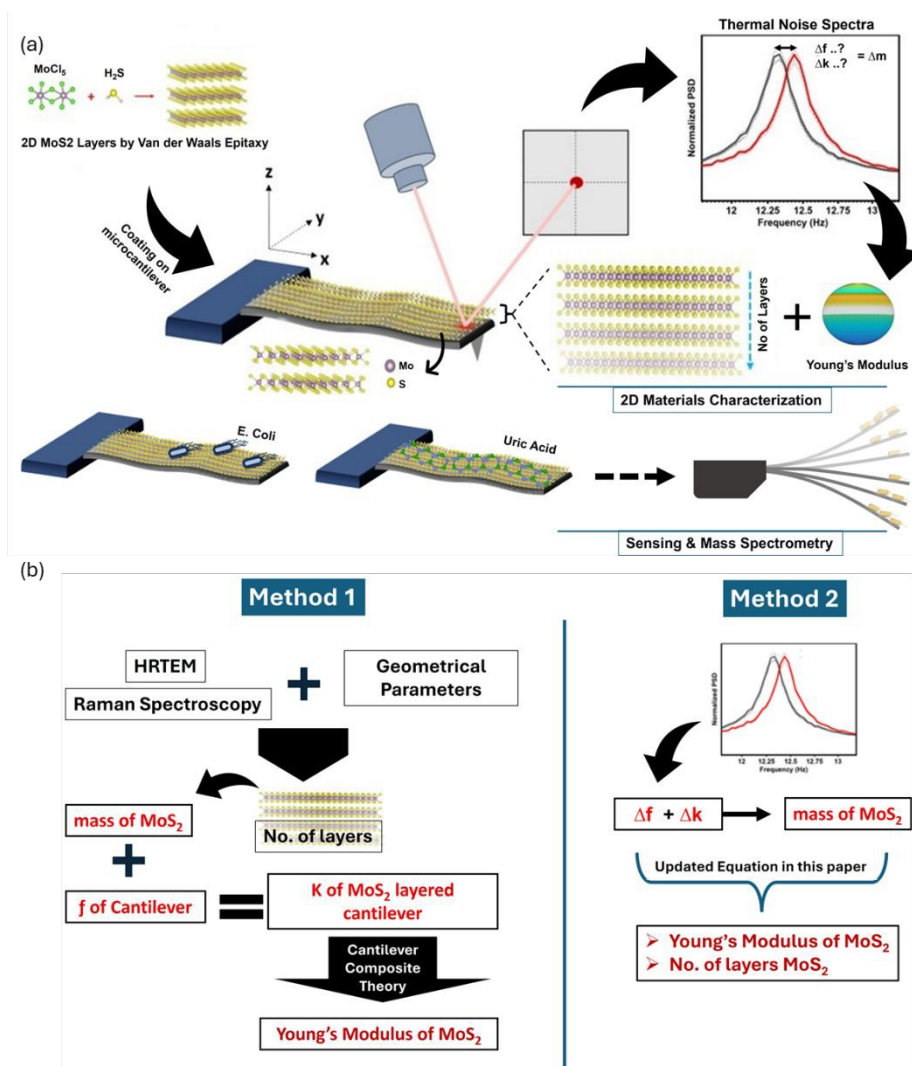


Fig. 1. (a) The schematic of the MoS₂ coating approach and methodology for sensing and characterization. In this work, we utilized the Van der Waals epitaxy method to synthesize 2D materials layers (e.g. MoS₂) and then transferred it over microcantilevers. The thermal noise spectra before and after deposition were recorded to measure the frequency shift and spring constant of microcantilever before and after deposition. Here we deconvoluted the mass and stiffness using an analytical model to measure the mass, layer thickness, and the number of layers of the added MoS₂ layer and its Young's modulus. The coated cantilever was finally used as a sensor to measure the mass of *E. coli* bacteria and Uric acid concentration in PBS buffer. (b) The schematic of the two methods used for characterization of coated MoS₂. In the first approach, the layers of coated MoS₂ are measured by Raman spectroscopy or/and HRTEM, then using cantilever geometry the mass of MoS₂ is calculated. Then, employing measured mass and frequency of coated microcantilever, the spring constant is calculated and used to compute the Young's modulus of MoS₂. In the second approach, by measuring the spring constant and mass of microcantilever before and after deposition, the mass of MoS₂ is measured and alongside the measured frequency and spring constant is used to measure the MoS₂ Young's modulus.

The cantilever is singly clamped at one end and free at the other end. The length of the cantilever is L_c , width b_c and thickness h_c oriented with the x-axis with flexural displacement along the z-axis. The coated MoS₂ has the same length and width as the cantilever and its thickness is h_a .

By neglecting rotary inertia and shear deformation, using the Galerkin discretization³⁰ and equalizing the mean values of the cantilever flexural work and kinetic energy per oscillation cycle, the resonance frequencies of the cantilever can be obtained as (see S1 in the supplementary materials):



$$\omega_n = \sqrt{\frac{\int_0^L EI_{eq} \psi_n^2 dx}{\int_0^L (\rho_c h_c + \rho_a h_a) \psi_n^2 dx}}$$

Where $\varphi_n(x)$ is the n^{th} eigenmode shape of the cantilever to satisfy the boundary conditions³¹, ω_n is the n^{th} eigenfrequency of the cantilever, ρ_c and ρ_a are the densities of the pristine cantilever and added layer, respectively. EI_{eq} is described as^{32–34}:

$$EI_{eq} = \frac{E_c h_c^3}{3} + \frac{E_a h_a^3}{3} + E_c h h_c (h - h_c) + E_a h_c h_a (h_c + h_a - 2h) + E_a h h_a (h - h_a) \quad (2)$$

Where E_c and E_a are Young's moduli of cantilever and added layer, respectively, and h is the position of the neutral axis because of the added top layer thickness:

$$h = \frac{E_c h_c^2 + E_a (h_a^2 + 2h_a h_c)}{2(E_a h_a + E_c h_c)} \quad (3)$$

From equation (1), we can derive expressions for the critical Young's modulus or critical density of the added layer that will increase the resonant frequency (see supplementary materials, S1):

$$EI_{eq} > \frac{E_c h_c^2 (h_c + h_a \frac{\rho_a}{\rho_c})}{12} \quad (4a)$$

And

$$\rho_a < \frac{12\rho_c EI_{eq}}{E_c h_c^2 h_a} - \rho_c \frac{h_c}{h_a} \quad (4b)$$

Furthermore, we consider the tip mass effect on our analysis of the cantilever dynamics.

Considering the tip mass in the Euler-Bernoulli equation³⁵, the characteristic equation is obtained as:

$$\kappa^3 (1 + \cos(\kappa) \cos h(\kappa)) + \frac{m_{tip} \kappa^4}{(\rho_c h_c + \rho_a h_a) b_c L_c} (\sinh(\kappa) \cos(\kappa) - \sin(\kappa) \cosh(\kappa)) \quad (5)$$

Where m_{tip} is the tip mass. Then, the frequency of cantilever is given by:

$$f_n = \frac{\kappa^2}{2\pi L_c^2} \sqrt{\frac{EI_{eq}}{(\rho_c h_c + \rho_a h_a)}} \quad (6)$$

Results and Discussion

Initially, to investigate the effect of tip mass on the frequency response of cantilever, we assume the tip mass is between 0 to 15% of the cantilever mass and performed numerical simulations. The results of the first to fourth eigenfrequencies are given in Figure 2. As can be seen, for the case that the tip mass is less than 10% of the cantilever mass, which is the case of commercial cantilevers, the tip mass effect is negligible. As Figure 2 shows, while increasing the thickness of deposition (here MoS₂) significantly increases the frequency of the cantilever, increasing the mass of the tip has negligible effect (less than 1%) on the frequency response of cantilever for all eigen-frequencies which means we can neglect its effect on our analysis of the cantilever dynamics.



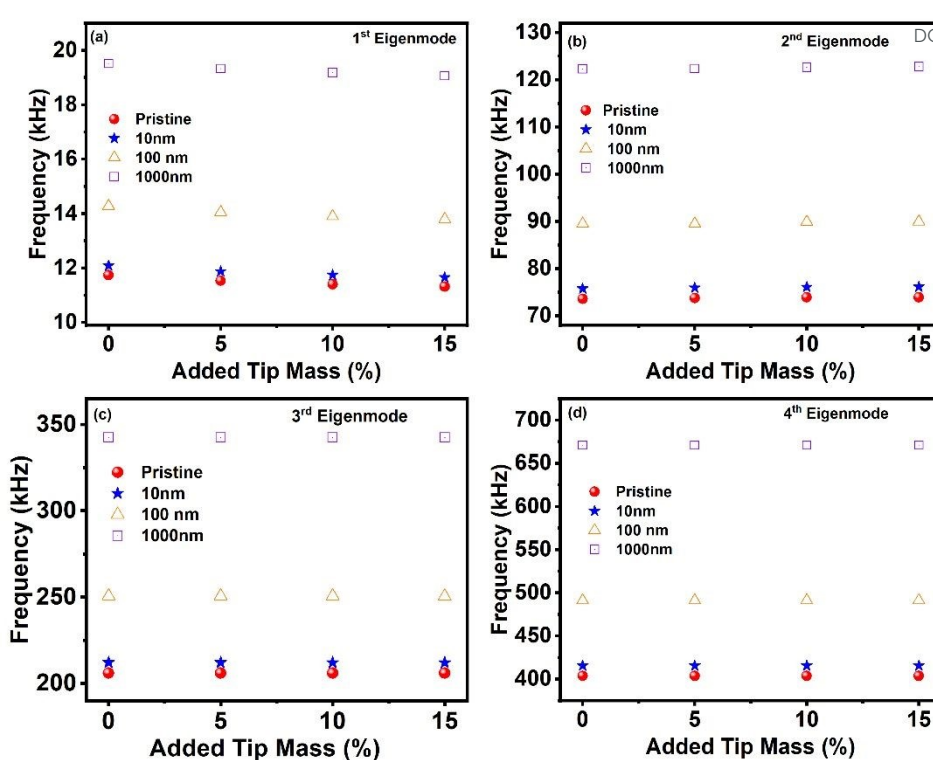


Figure 2. Study of the effect of tip mass on the eigen-frequencies of a microcantilever with different coating thickness. (a) The first eigenfrequency, (b) second eigenfrequency, (c) third eigenfrequency and (d) fourth eigenfrequency. The thickness of the coating is varied from 10 nm to 1000 nm. Increasing the thickness of the coating leads to an increase of frequency as the coated material is MoS_2 , which is stiffer than the cantilever material (here, silicon).

Then, our combined model is employed to analyze how the thickness and properties of coated materials impact the frequency response of a microcantilever. We conducted calculations to determine the variations in the natural frequency of the modified cantilever as materials with different Young's modulus and density were deposited on the pristine cantilever. In this study, we focused on two silicon-based microcantilevers, namely SCM-PIC and FMV-A. Although the material properties of both cantilevers are identical, their geometry (length, width, and height) differ. The calculations were performed across a range of added material thicknesses, and the results are illustrated in Fig. 3a and Fig. 3b.

In our observations, we identified a specific density and Young's modulus combination where the polarity of the frequency shift is reversed. We designated this particular frequency as the critical frequency, and the corresponding density and Young's modulus values as critical density and critical Young's modulus, respectively. Additionally, our findings indicate that increasing the thickness of added materials results in a positive frequency shift. The magnitude of this frequency shift is more pronounced in the FMV-A cantilever compared to SCM-PIC, reflecting the higher sensitivity of the FMV-A microcantilever. This responsivity can be attributed to the fact that the critical frequency, critical density, and critical Young's modulus are significantly influenced by the type of pristine cantilever and its geometry.



In order to visualise these in a better and simpler way, we have plotted 2D contour plots for 2 different cantilevers, SCM-PIC and FMV-A and represented them in Fig. S1 (Supplementary materials, section S2).

In the preceding section, our aim is to investigate how the original cantilever's geometry influences frequency shifts. To expand our analysis and explore the influence of material properties of the pristine cantilever on frequency shifts resulting from layer deposition, we utilized a silicon nitride-based QUEST R 200 cantilever. We then plotted the changes in the natural frequency of the modified cantilever as materials with varying Young's modulus and density were deposited onto the pristine cantilever at different thickness levels (Fig. S2). The observed variation was similar to that of the silicon-based cantilevers, but the magnitudes of frequency shifts were higher compared to the silicon-based ones, indicating the higher responsivity of the QUEST R 200 cantilever.

To summarize our simulations (Figure 3, Figures S1-S2), we can mention that in our study, we simulated MoS₂ coating on three types of cantilevers:

- SCM-PIC (silicon): length 450 μm , thickness 2.5 μm , spring constant ~ 0.2 N/m
- FMV-A (silicon): length 225 μm , thickness 2.5 μm , spring constant ~ 2 N/m
- Quest R 200 (silicon nitride): length 200 μm , thickness 900 nm, spring constant ~ 0.2 N/m

Despite SCM-PIC and Quest R200 having comparable stiffness (~ 0.2 N/m), the frequency shift upon MoS₂ deposition was consistently larger for Quest R200. This can be attributed to their significantly different effective masses. SCM-PIC is both longer and thicker than the Quest R200, which results in a higher effective mass. Since the relative frequency shift is governed by mass and stiffness changes, a higher cantilever mass leads to a smaller relative frequency shift. As a result, for the same MoS₂ coverage, Quest R200—with its smaller mass—undergoes a larger fractional frequency shift than SCM-PIC. Thus, even with similar stiffness, geometry, and material differences lead to substantially different frequency responses.

The second silicon cantilever, FMV-A, further highlights this contrast. It has slightly longer length (225 μm) than Quest R200 (200 μm) but is much stiffer (~ 2 N/m) and thicker (2.5 μm). Consequently, FMV-A exhibits the largest effective mass and lowest compliance changes among the three. As predicted by resonance theory, its frequency response to surface loading is minimal.

This is the prime reason for the highest frequency shift in the case of the QUEST R 200 cantilever. Furthermore, as can be seen from Figure 3, S1 and S2, as we have used 2D materials with high Young's modules, in most cases we observe positive frequency shift which can be related to the dominance of stiffness changes than mass changes in the deposited microcantilevers and by increasing the thickness of deposited materials, the positive frequency shift is increased.



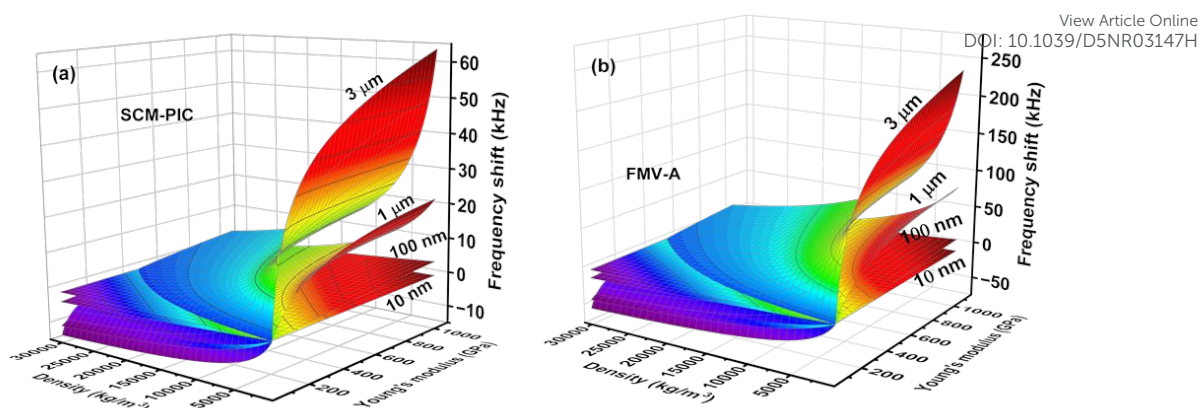


Fig. 3. 3D plots obtained from the numerical simulation results of frequency shift due to the changes of Young's modulus and density of coated bulk materials on the microcantilever surface with different coating thicknesses for the SCM-PIC cantilever and the FMV-A cantilever. (a) Represents the changes in frequency shift for the SCM-PIC cantilevers where the coating thicknesses were 10 nm, 100 nm, 1 μm , and 3 μm , respectively. (b) Represents the changes in frequency shift for SCM-PIC cantilevers where the coating thicknesses were 10 nm, 100 nm, 1 μm , and 3 μm , respectively.

In the subsequent step, we validate the analytical equations for calculating critical values (equations 4a and b) by comparing them with the corresponding numerical simulation results. For this comparison, we focused on extreme case height scenarios, with the coated layer thickness considered at 10 nm and 3 μm , respectively.

The variations of critical density against ranges of Young's modulus and critical Young's modulus against different densities are calculated for three cantilevers: (a) FMV-A and (b) QUEST R 200 (depicted in Figs 4 a-d), and (c) SCM-PIC (Supplementary Fig. S3a and Fig. S3b).

The results reveal a remarkable alignment between numerical simulations and the analytical equations. Through this analysis, we observed that, for lower added layer thickness, the FMV-A cantilever achieved a critical density at a relatively higher value compared to the QUEST R 200 cantilever for the same coated Young's modulus (Fig. 4a). The variation is linear at lower heights but exhibits significant non-linearity for a thicker added layer (3 μm). Furthermore, for the thicker height, the behavior of both cantilevers reversed, with the FMV-A cantilever attaining a lower critical density than the QUEST R 200 cantilever at the same Young's modulus (Fig. 4b).

Concerning the critical Young's modulus for the low height of the added layer, similar to the critical density, we observed a linear relationship. For the same density of the added layer, the FMV-A cantilever reached the critical Young's modulus at a lower value (Fig. 4c). Although the cantilevers exhibited non-linearity for the 3 μm height, in this case, the QUEST R 200 cantilever reached the critical Young's modulus at a lower value compared to the FMV-A cantilever (Fig. 4d). The variations for the SCM-PIC cantilever are almost identical to those of the FMV-A cantilever (Supplementary Figs. S3a and S3b) since both cantilevers share similar material properties.

Our analysis thoroughly explores the complex interaction of critical Young's modulus, density, and coating layer thickness, revealing a nonlinear coupling effect that impacts the direction of frequency shift in coated microcantilevers. Additionally, considering the different density and Young's modulus



of silicon and silicon nitride as the materials of FMV-A and QUEST R 200 microcantilevers, this phenomenon is closely linked to the inherent stiffness and mass of the pristine microcantilever. Furthermore, our modeling approach and results can serve as a guideline for elucidating the anomalous frequency shifts observed in microcantilevers coated with various materials. This section can be summarized as:

The phenomenon of frequency shift polarity reversal arises from the interplay between two competing effects induced by the coating: (1) the added mass loading, which tends to *decrease* the resonance frequency, and (2) the effective stiffness enhancement, which tends to *increase* it. The net result of coating a cantilever depends on which of these two opposing contributions dominate.

When a thin film is deposited on the cantilever, the total mass increases due to the film's mass per unit area, which scales linearly with the density and thickness of the film. Simultaneously, the stiffness of the cantilever is altered, since the film also contributes to the bending rigidity of the composite structure. The degree of this enhancement depends on the Young's modulus and the film's position relative to the neutral axis, and scales strongly with thickness.

Thus, a coating with high density and low Young's modulus will primarily increase the effective mass without contributing significantly to stiffness, resulting in a negative frequency shift (downshift). Conversely, a coating with high Young's modulus and relatively low density can increase stiffness more than the mass, yielding a positive frequency shift (upshift).

The combination of density and Young's modulus at which this crossover happens defines the critical values—the *critical density* and *critical Young's modulus*—for a given cantilever geometry and film thickness. This is why we observe a well-defined point of polarity reversal that is sensitive to the coating's mechanical properties and the cantilever's dimensions.



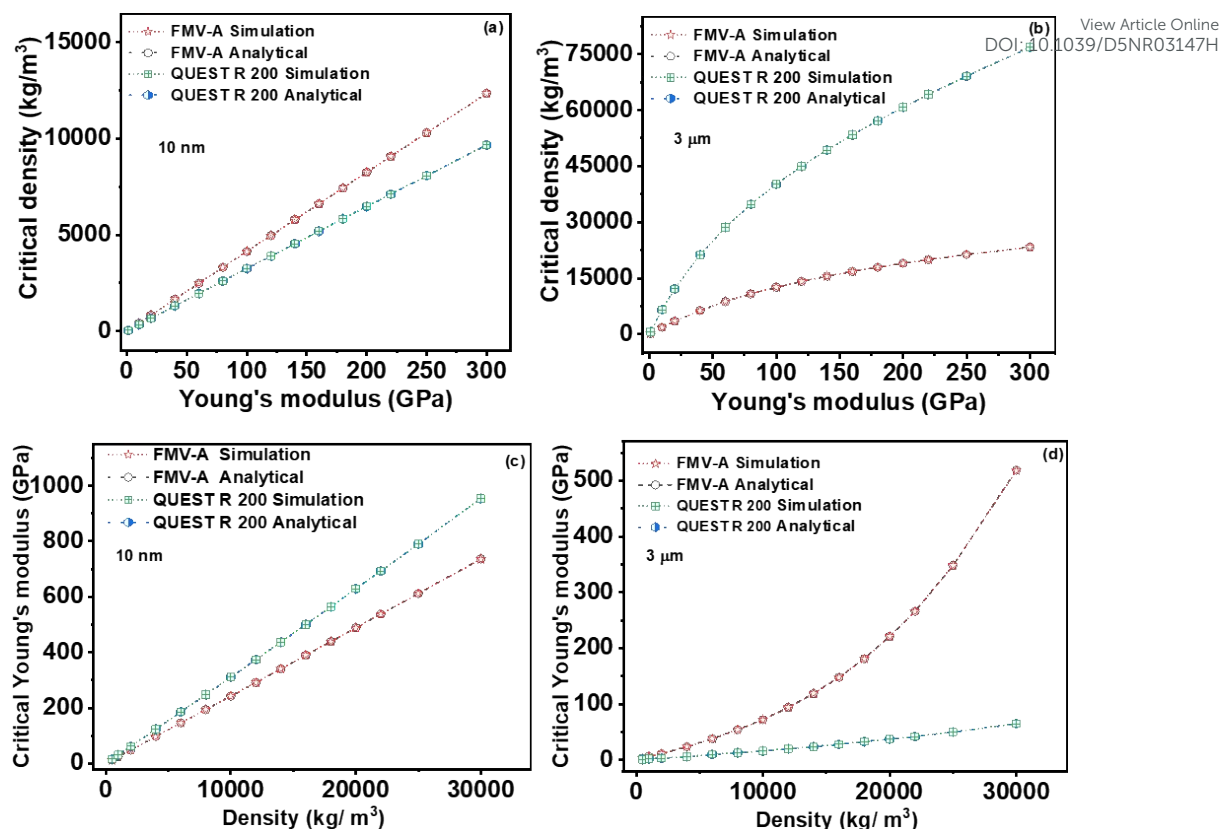


Fig. 4. Comparison between the critical density and Young's modulus obtained from numerical simulations and developed analytical equations. (a) and (b) are the critical densities vs Young's modulus for QUEST R 200 and FMV-A cantilevers for 10 nm and 3 μm added layer thickness, respectively. (c) and (d) the critical Young's modulus vs densities for QUEST R 200 and FMV-A cantilevers for 10 nm and 3 μm added layer thickness, respectively.

Having established the generality of our analytical model for bulk materials, we extended our investigation to the domain of 2D materials, which exhibit unique mechanical and electronic properties. To this end, we parameterized our simulation with the material properties—including Young's modulus, density, and interlayer distance—of several prominent 2D materials: tungsten diselenide (WSe₂), tungsten disulfide (WS₂), titanium disulfide (TiS₂), molybdenum diselenide (MoSe₂), graphene, and hexagonal boron nitride (hBN) (See their parameters we used in our simulation in the materials and methods section). We then systematically calculated the fundamental eigenfrequency shift (f_1) as a function of the number of deposited layers for two distinct commercial cantilevers, the SCM-PIC and the FMV-A, to assess both the material-dependent response and the cantilever sensitivity. The results of this comprehensive parametric sweep are presented in Fig. 5a and 5b, with a detailed analysis of the frequency shift for each specific 2D material as a function of layer number further provided in Figs. S4a and S4b.

The simulations revealed a clear contrast in the cantilever response. For WS₂, TiS₂, graphene, and hBN, the eigenfrequencies of the modified cantilevers were higher than those of the pristine ones, indicating a positive frequency shift. In contrast, the frequencies of cantilevers coated with MoSe₂ and WSe₂ were lower, demonstrating a negative frequency shift. This can be explained by the dominance of mass



changes over stiffness changes for MoSe₂ and WSe₂ coated microcantilevers, attributed to their lower Young's modulus and higher density compared to the other materials.

To quantify this effect, we plotted the frequency shift for 20 layers of each material. For the SCM-PIC cantilever, positive frequency shifts of 87 Hz, 102 Hz, 372 Hz, and 322 Hz were observed for WS₂, TiS₂, Graphene, and hBN, respectively. For MoSe₂ and WSe₂, negative frequency shifts of 10 Hz and 33 Hz were obtained. The FMV-A cantilever followed a similar trend but with a higher frequency shift, confirming its greater sensitivity. For the FMV-A, a 20-layer deposition of graphene yielded the highest positive frequency shift of 1.425 kHz, while WSe₂ produced the highest negative shift of 127 Hz. Positive shifts of 336 Hz, 390 Hz, and 1.23 kHz were observed for WS₂, TiS₂, and hBN, respectively, and a negative shift of 38 Hz was observed for MoSe₂.

The model's sensitivity extends to the monolayer limit, as detailed in Fig. 5c and 5d. For the SCM-PIC, the monolayer frequency shifts were +4.5 Hz (WS₂), +5 Hz (TiS₂), +16.4 Hz (hBN), and a maximum of +19 Hz for graphene, while MoSe₂ and WSe₂ produced negative shifts of -0.5 Hz and ~-2 Hz, respectively. For the more sensitive FMV-A cantilever, the monolayer shifts were +18 Hz (WS₂), +20 Hz (TiS₂), +66 Hz (hBN), and a maximum of +72 Hz for graphene, with MoSe₂ and WSe₂ showing negative shifts of -2 Hz and ~-7 Hz, respectively. These findings not only validate the predictive power of our model across diverse material systems but also provide a quantitative guide for selecting or synthesizing 2D materials to achieve a desired frequency response in coated microcantilevers.



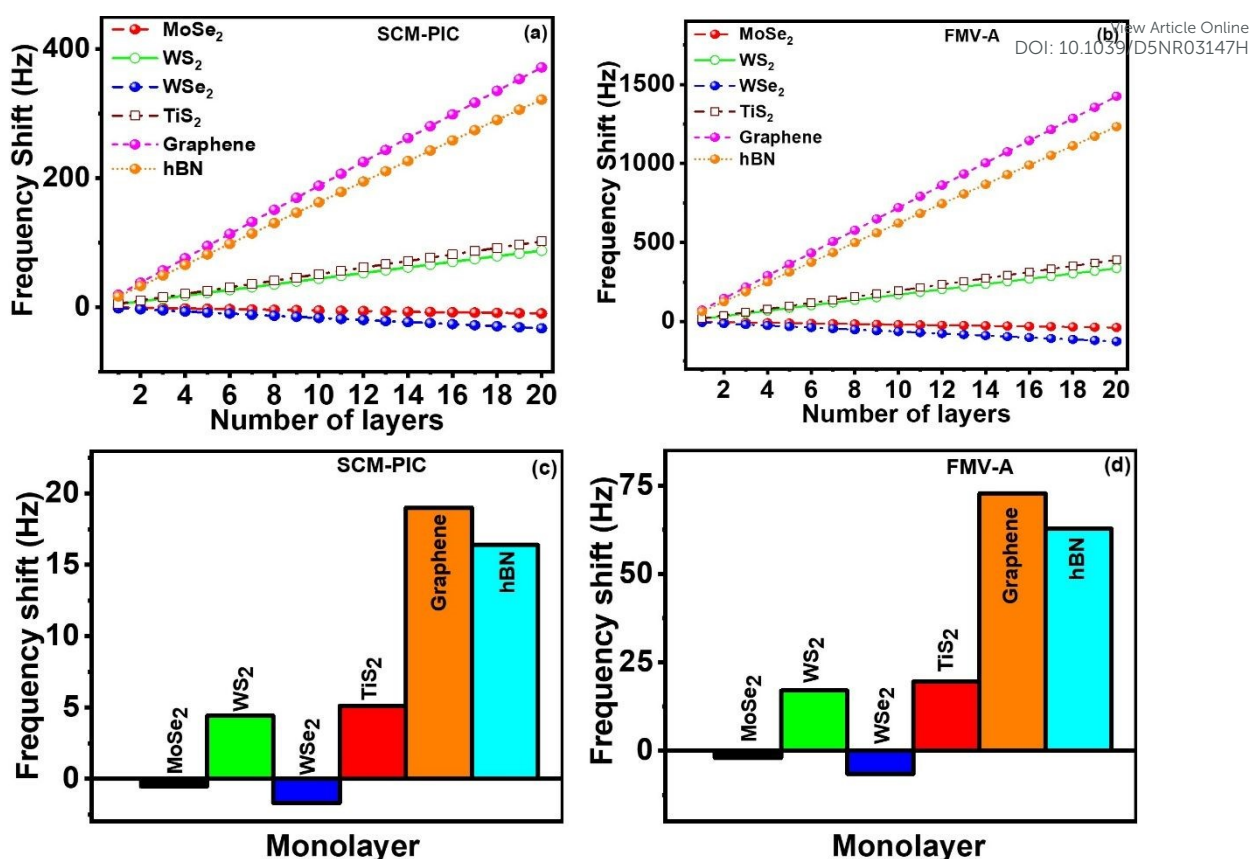


Fig. 5 (a) and (b) the frequency shifts of SCM-PIC and FMV-A cantilevers for different 2D materials and different numbers of 2D materials' layers. (c) and (d) the frequency shift of SCM-PIC and FMV-A cantilevers for monolayer 2D materials.

Experimental Section

We applied the developed equations to quantify the mass, thickness, number of layers, and Young's modulus of 2D materials. Additionally, we demonstrated our experimental approach for coating the microcantilever surface with 2D materials to precisely control the cantilever's resonant frequency for sensing applications. In this context, we modified the SCM-PIC, PPP-NCH and TAP300DLC cantilevers by coating their surface with MoS₂ using the Van der Waals epitaxy technique (VdWE), followed by a transfer process^{26,27,36}. In our 2D materials transfer process, we avoided using harsh chemicals to etch the substrate. Instead, we used only high-purity DI water to separate the 2D materials from the substrate (300nm SiO₂/Si). Additionally, the 2D materials were supported with PS on a TR frame, ensuring that only the 2D materials/PS film came into contact with the cantilever. To remove the PS, we used high-purity chloroform, which has the best solubility for PS, in a sealed container for 48 hours. This ensured no PS residue remained on the cantilevers. Finally, the cantilevers with the 2D materials were further rinsed with chloroform.

The as-grown MoS₂ samples were then characterized using High-Resolution Transmission Electron Microscopy (HRTEM), Raman spectroscopy and X-ray photoelectron spectroscopy (XPS). The thickness and number of layers of the as-grown MoS₂ specimen were measured using HRTEM and are



represented in Fig. 6a. Between 5-7 layers of MoS₂ sheets were observed and a layer thickness of 0.65 nm was measured, which matches nicely with the values reported in the literature³⁷.

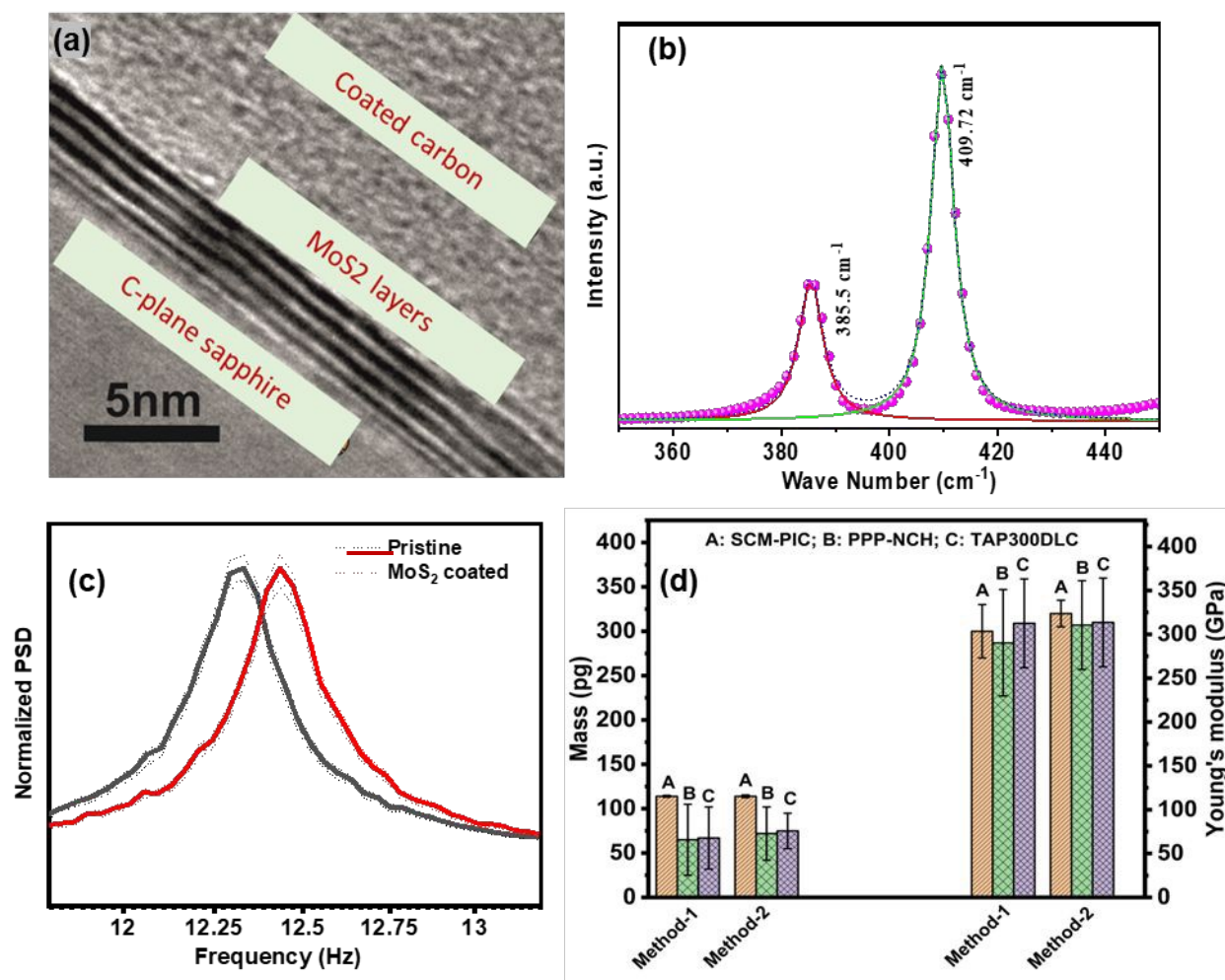


Fig. 6. (a) HRTEM image of as-synthesized MoS₂ sample. (b) Raman spectrum of a few-layer MoS₂ coated on SCM-PIC cantilever highlighting the E_{2g} and A_{1g} vibrational bands. (c) Normalized thermal Noise spectra of Pristine SCM-PIC (black line) and MoS₂ coated SCM-PIC (red line) cantilever highlighting the 1st eigenfrequencies of the cantilevers and (d) the measured values of mass (yellow bars) and Young's modulus (blue bars) of the deposited few layers of MoS₂ calculated with method 1 and method 2 for: A: SCM-PIC, B: PPP-NCH, and C: TAP300DLC cantilevers.

Raman spectroscopy is considered to be the fingerprint to obtain the number of layers of any MoS₂ sample. From the difference between the wavenumbers of the vibrational peaks corresponding to E_{2g} and A_{1g}, one can obtain valuable information about the number of layers corresponding to the MoS₂. In our measurement, we measured the Raman spectra utilizing a 532 nm laser system and considered different parts of the added layer on all three cantilevers. The average difference between the two peaks for the SCM-PIC cantilever is calculated as $\sim 24.3 \pm 0.1 \text{ cm}^{-1}$ (Fig. 6b). For the PPP-NCH and TAP300DLC cantilevers the values are calculated as $\sim 24.1 \pm 0.1 \text{ cm}^{-1}$ and $\sim 24.0 \pm 0.1 \text{ cm}^{-1}$ respectively (Fig. S5a and S5b). All these wavenumber shifts correspond to 5-7 layers^{38,39}.



The X-ray photoelectron spectroscopy (XPS) was carried out to characterize the compositions of these VdWE-grown MoS₂ layers to investigate two core levels, Mo 3d and the S 2p of the as-synthesized MoS₂ and the result is represented in Fig. S6A (a) and Fig. S6A (b). As shown in Fig. S6A (a), two MoS₂ peaks (dark blue), Mo (IV) 3d_{3/2} and Mo (IV) 3d_{5/2}, were found at 232.8 eV and 229.6 eV, respectively. In the same spectrum, S 2s peak (pink) was observed at 226.8 eV, and a peak at 236.3 eV was assigned to the Mo (VI) 3d_{3/2} (light blue), indicating a small amount of oxidation, which resulted from the sample being exposed to the ambient environment. It should be noted that a Mo (VI) 3d_{5/2} peak overlaps with Mo (IV) 3d_{3/2} at 232.8 eV. For the MoS₂ S 2p core level, two peaks (pink) labelled in Fig. S6A (b) as S 2p_{1/2} and S 2p_{3/2} corresponding to MoS₂ were found at 163.6 eV and 162.4 eV, respectively. In addition, with a semi-quantitative method to investigate the ratio of elements, the atomic ratio of S/Mo was found to be close to 2 with a slight S deficiency.

To further verify the extent and uniformity of the MoS₂ coating, we conducted field emission scanning electron microscopy (FESEM) combined with energy-dispersive X-ray spectroscopy (EDAX) (Fig. S6 B). Figure S6 B clearly shows the presence of molybdenum (Mo) and sulfur (S) across the surface of the originally Al-coated Si cantilever, confirming the spatial distribution of the coating.

To further assess the uniformity and thickness of the MoS₂ film, Raman spectroscopy was performed at multiple locations along the coated cantilevers (Fig. S6 C). The observed peak positions and inter-peak separations were consistent across different regions, indicating a uniform number of MoS₂ layers and confirming the reproducibility of the coating. The number of layers estimated from Raman spectra (5–7 layers) is in good agreement with our HRTEM analysis, which provides a direct measure of the MoS₂ thickness.

After preparing the MoS₂-coated microcantilevers, we measured the frequency response of the coated microcantilevers and compared them with their pristine counterparts. First, we implemented the methodology presented on the SCM-PIC cantilever and then we extended that on PPP-NCH and TAP300DLC cantilevers.

The thermal noise spectra of pristine SCM-PIC and MoS₂-coated SCM-PIC cantilevers are recorded and plotted in Fig. 6c. The first eigenmode of the pristine and coated cantilevers was measured to be 12.32 ± 0.05 kHz and 12.44 ± 0.02 kHz, respectively. In this case, we observed the frequency of the pristine cantilever is lower than that of the coated cantilever which shows the dominance of stiffness changes than mass changes when MoS₂ is coated on the microcantilever which can be explained by high Young's modulus of MoS₂.

As mentioned in the introduction, to calculate the mass, Young's modulus and thickness of deposited MoS₂ on the microcantilevers we have used two methods (Fig 1b):

In the first method, by knowing the number of layers and thickness of the coated MoS₂ from HRTEM and Raman spectroscopy measurements, we can calculate the mass of the coated MoS₂ microcantilevers from the geometrical parameters of the cantilever. The obtained mass from the geometrical parameters of the microcantilever (supplementary materials, equation S5) is 114 ± 0.5 pg. Then, we use equations



(1)-(3) to measure the Young's modulus of deposited MoS₂. The value we obtained is $305 \pm 30 \text{ GPa}$ (we called this way method 1). View Article Online
DOI: 10.1039/D5NR03147H

In the second method, based on our approach that we consider the variation of both stiffness and mass of the microcantilever due to the coating of the layer on its surface and our ability to measure the spring constant of the coated microcantilever, we use the following equation to not only measure the mass of deposited MoS₂ but also directly measure the number of layers of the 2D material using the microcantilever via decoupling the mass and stiffness changes effect from the measured frequency shift:

$$\Delta m = \frac{1}{4\pi^2} \left(\frac{k_N}{f_N^2} - \frac{k_{N+\Delta f_N}}{(f_N \pm \Delta f_N)^2} \right) \quad (7)$$

Where k_N is the spring constant of pristine cantilever and $k_{N+\Delta f_N}$ is the spring constant of the coated MoS₂ microcantilever. In equation (7), f_N is the resonance frequency of the pristine cantilever and Δf_N is the frequency shift between pristine and modified cantilever.

The mass of deposited MoS₂ is calculated as $114 \pm 0.2 \text{ pg}$ which corresponds to 5 to 7 layers of MoS₂ and is the same as the value we obtained by knowing the number of layers from HRTEM and Raman spectroscopy. It not only proves the accuracy of the presented methodology but also depicts the capability of microcantilevers to measure directly the number of layers of 2D materials.

Worth mentioning that the measured spring constant of pristine and MoS₂-coated microcantilevers are $0.16 \pm 0.06 \text{ N/m}$ and $0.17 \pm 0.05 \text{ N/m}$, respectively.

By measuring the spring constant of MoS₂ coated microcantilever, we can use equation (S4) as well as equations (2) and (3) to measure the Young's modulus of deposited MoS₂ (we called this approach method 2). The obtained value is $315 \pm 15 \text{ GPa}$ which is similar to the values calculated from method 1 and matches well with the reported values in the literature^{40–42}.

To show the generality and repeatability of our measurement, we then used the other two MoS₂-coated cantilevers (PPP-NCH and TAP300DLC) and measured the mass and Young's modulus of the added MoS₂ layer. The mass of the added MoS₂ layer for the PPP-NCH cantilever was found to be $65 \pm 40 \text{ pg}$ (method 1) and $72 \pm 30 \text{ pg}$ (method 2). Similarly, the mass obtained from the TAP300DLC cantilever was calculated to be $67 \pm 35 \text{ pg}$ (method 1) and $75 \pm 20 \text{ pg}$ (method 2). Young's modulus of the added MoS₂ layer for the PPP-NCH cantilever was found to be $287 \pm 60 \text{ GPa}$ (method 1) and $309 \pm 50 \text{ GPa}$ (method 2). Accordingly, the Young's modulus obtained of the added MoS₂ layer for the TAP300DLC cantilever was calculated to be 307 ± 5 (method 1) and $310 \pm 50 \text{ GPa}$ (method 2).

The mass of deposited MoS₂ obtained from measuring the number of layers from HRTEM, Raman spectroscopy (method 1) and equation (7) (method 2) are given in Fig. 6d (yellow bars). Also, the obtained Young's modulus of MoS₂ coating from equations (1)-(3) by knowing the number of layers from HRTEM and Raman spectroscopy (method 1) and also from equation (7) and equation (S4) (method 2) are given in Fig. 6d (blue bars).



As to quantify the mass, number of layers and Young's modulus of deposited MoS₂ layers, the geometrical parameters of cantilevers would be involved, due to the variations of actual length, width and height of microcantilevers from their nominal values provided by manufacturers, we have performed integrated simulation-experiments analysis to probe the effects of their variations on the measured frequency response and frequency shift of both pristine and modified cantilevers. For this analysis, we utilized the three different cantilevers: (a) SCM-PIC, (b) FMV-A, and (c) PPP-NCH, with their nominal values provided in the Materials and Methods section. In the subsequent step, we measured their actual dimensions using Scanning Electron Microscopy (SEM) and consequently determined their resonance frequency via thermal noise spectra analysis (see Figure S7). It is noteworthy to mention that the spring constants were calibrated from the thermal noise spectra as well, using Sader's method⁴³.

In our simulation, we assessed the impact of dimensional variations on the cantilevers, considering a maximum length change of 10% of their nominal length, a maximum width change of 33% of their nominal width, and a maximum thickness change of 25% of their nominal thickness. These variations are significantly higher than the actual measured changes⁴⁴. We then analyzed the frequency changes resulting from these dimensional variations for both the pristine and the modified cantilevers. The resonance frequencies at nominal values, as well as the shifts due to dimension variations, are depicted in Supplementary Figure S7. The figure clearly illustrates that while the frequencies of both pristine and modified cantilevers are influenced by dimensional variations, the frequency shift caused by the added MoS₂ layer remains relatively constant across all variations.

Furthermore, in our quantification of the mass, number of layers, and Young's modulus of MoS₂ layers coating, represented in Figure 6dd, we included error bars to account for the uncertainties in the cantilever geometry used in the quantification.

It's noteworthy that for all our thermal noise measurements and simulations, we specifically opted for the nominal values of cantilevers rather than their actual values. As mentioned, in our analysis we explored the deviations of cantilever dimensions from their nominal values and tracked their resonance frequencies accordingly. Furthermore, Fig. S7d provides a comprehensive plot depicting the percentage changes in frequency corresponding to percentage changes in height specifically for the PPP-NCH cantilever. We used a similar approach in determining the frequency shifts as a function of the deviation of other dimensions for all the cantilevers.

To complement our simulation findings, we conducted experimental measurements of several cantilevers using scanning electron microscopy (SEM). These measurements revealed that the actual dimensions of all examined cantilevers fell within the range of deviations considered in our simulation methodology. Highlighting the real dimensions of the PPP-NCH cantilever, Fig. S7e and S7f present a representative SEM image. The measured length and width of this cantilever were found to be 132.5 μm and 40.2 μm , respectively, while the thickness was measured to be 3.8 μm .



Furthermore, it is worthy to mention that in our error analysis, we considered a range of measured layers of MoS₂ by HRTEM and Raman spectroscopy, variations in measured frequency and spring constant before and after deposition using thermal spectra as well as the error range in the cantilever parameters as discussed above. For this reason, we provide the average and max/min values for measured mass and Young's modulus.

Next, to show and compare the performance of our proposed MoS₂-coated microcantilevers in sensing applications, we have used our modified microcantilevers to measure the mass of antibiotic-resistant (ABR) *E. coli* bacteria as well as different concentrations of Uric acid.

It should be noted that in our sensing experiments, we follow our previous work²⁵, in which the cantilever was not fully immersed in liquid during these experiments. Instead, a thin droplet of PBS buffer was carefully placed atop the cantilever surface, resulting in a thin liquid film on the surface of cantilever rather than full submersion. Because of this, the added mass and hydrodynamic loading from the bulk liquid are minimal compared to full immersion scenarios.

For the measurement of the mass of ABR *E. coli*, we grew a culture of ABR *E. coli* and resuspended the bacteria in a phosphate-buffered saline (PBS) buffer solution. To determine the mass of the *E. coli* we first considered the effect of the PBS layer. In our experimental setup, we deposited 5 µl of PBS on both cantilevers. In the next step, we deposited 5 µl of the bacteria suspended in PBS over the pristine and modified cantilever and for all the cases we monitored the 1st eigenfrequencies obtained from the thermal noise spectra (Figs. 7 a and b). The concentration of *E. coli* was determined via a plate count method with an average of 5416 ± 861 colony forming units (CFU), the reported mass of an *E. coli* cell is 1048 ± 98 fg (~ 1 pg)²⁸; therefore the mass in the sample is estimated to be $\sim 5.416 \pm 0.861$ ng.

In this part of our measurement, firstly we use the pristine and modified SCM-PIC cantilever as a potential mass sensor to quantify the mass of *E. coli* effectively and accurately.

In the case of the pristine cantilever, we observed a 3 Hz negative frequency shift when the PBS was deposited on the top of the cantilever. For the same amount of PBS, the MoS₂-coated cantilever exhibited a higher negative frequency shift of ~ 7 Hz. This confirms that the responsivity of the MoS₂-coated cantilever is higher than that of the pristine cantilever which can provide a more trustworthy frequency shift for the added PBS layer.

From both Figs. 7a and 7b and Fig. S8 (a-d), we observed a substantial frequency shift from the natural frequency of PBS layer-modified cantilevers. Frequency shifts of 75 Hz and 116 Hz (equivalent to 0.7% and 1% relative frequency shifts) were obtained from the pristine and MoS₂-coated SCM-PIC cantilever, respectively.

We then used equation (7) to determine the mass of the bacteria for both the cantilevers and compared the as-obtained mass from the CFU counts. The mass obtained by the CFU measurement, and from the frequency shift data for both the cantilevers are very close to each other while the modified microcantilever shows superior precision (Fig. 7d). Our results demonstrated that the mass of the added



bacteria can be measured effectively and accurately, indicating that the proposed 2D material-coated microcantilever functions as a highly responsive mass sensor.

Similar analyses were carried out using the PPP-NCH and the TAP300DLC cantilever (pristine and coated). The thermal noise spectra of all four cantilevers (two pristine and two modified) are represented in Fig. S8 (a-d). In this case, the mass of the *E. coli* bacteria obtained from the plate counts was measured as $\sim 15.016 \pm 3.0$ ng. The resonance frequencies of the cantilevers were found to be 310.1 kHz (PPP-NCH), 313.67 kHz (MoS₂-coated PPP-NCH), 295.32 kHz (TAP300DLC) and 297.48 kHz (MoS₂-coated TAP300DLC). Here also, we observed negative frequency shifts of 80 Hz (PPP-NCH), 176 Hz (MoS₂-coated PPP-NCH), 76 Hz (TAP300DLC) and 168 Hz (MoS₂-coated TAP300DLC) when the PBS was deposited on the top of the cantilevers.

On the other hand, frequency shifts of 9.1 kHz and 13.8 kHz (3% and 4.4% relative frequency shifts) were measured respectively for pristine and MoS₂-coated PPP-NCH cantilevers. Similarly, frequency shifts of 8.7 kHz and 11.68 kHz (2.94% and 3.92% relative frequency shifts) were measured respectively for pristine and MoS₂-coated TAP300DLC cantilevers. The significant changes in frequency shift for these two types of cantilevers can be explained by their significantly higher frequencies and their shorter length.

For these cantilevers as well, we observed that the responsivity of the modified cantilevers is greater than that of the pristine cantilever. Moreover, the obtained negative frequency shifts highlight the dominance of mass change rather than stiffness change in the microcantilever when PBS is added to its surface.

View Article Online
DOI: 10.1039/D5NR03147H



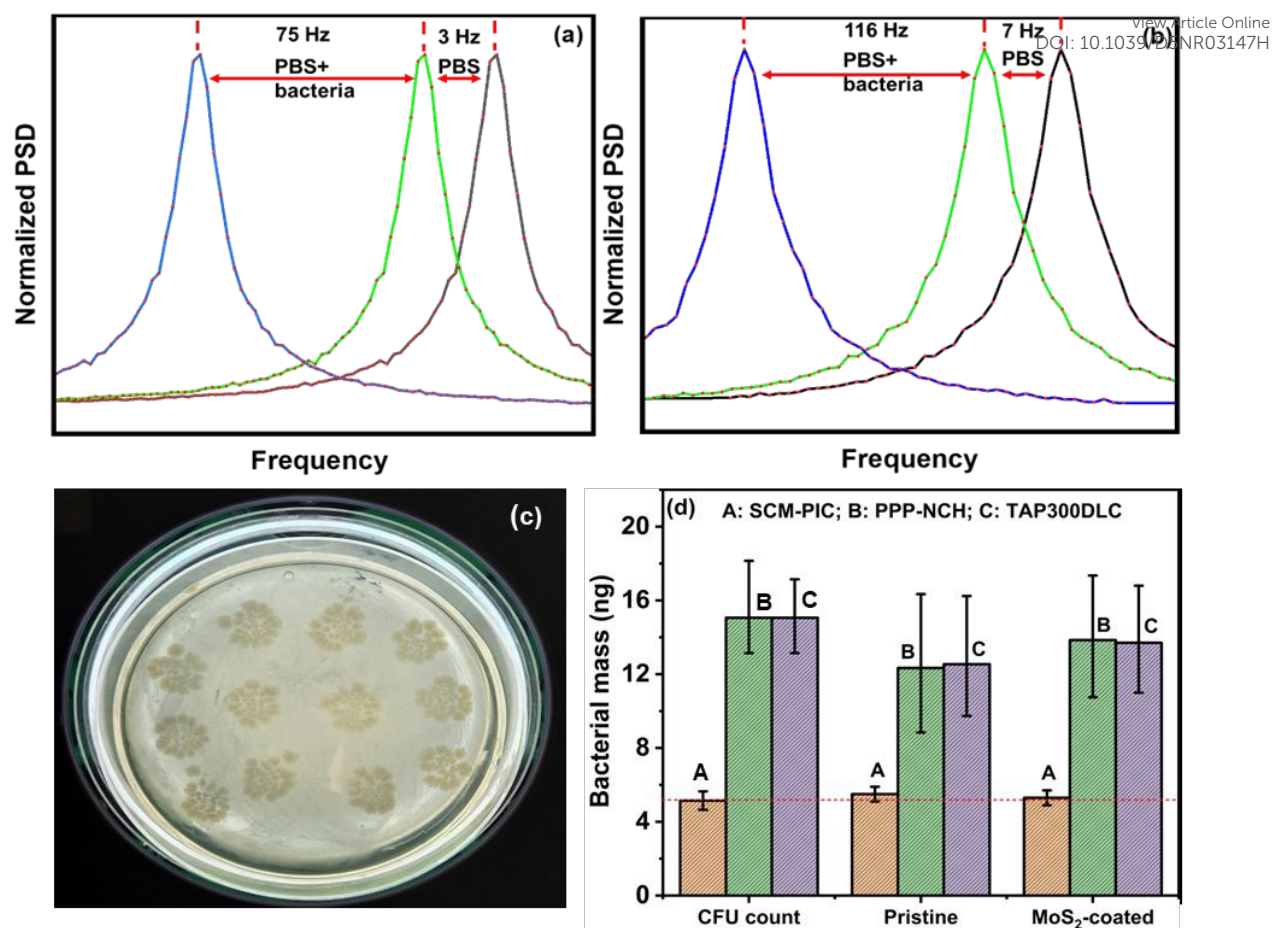


Fig. 7. (a) Thermal noise spectra for the pristine SCM-PIC cantilever in air, with PBS buffer, and *E-coli* bacteria in PBS. The first eigenfrequency of the pristine cantilever in the air was measured to be 11.413 kHz. (b) Thermal noise spectra for the MoS₂ coated SCM-PIC cantilever in air, with PBS buffer, and *E-coli* bacteria in PBS. The first eigenfrequency of the pristine cantilever in the air was measured to be 12.444 kHz. (Air = black, PBS Buffer = green, *E-coli* bacteria in PBS = blue) (c) Bacterial colony in Agar plate. (d) The calculated mass of the *E-coli* bacteria from CFU count and the frequency shift for pristine and MoS₂ coated cantilevers (A: SCM-PIC (orange), B: PPP-NCH (green) and C: TAP300DLC (purple)).

Uric acid plays multifaceted roles as a crucial biomarker, neurotransmitter, and antioxidant, necessitating its precise detection in bodily fluids. In the concluding phase of this investigation, our aim was to detect different concentrations of uric acid dissolved in PBS solution, ranging from 2 μM to 15 μM . We used both the pristine and MoS₂-coated cantilevers (PPP-NCH, and TAP300DLC) and measured the resonance frequencies and the corresponding spring constant. Then we employed two distinct mathematical methodologies (equation 7 and equation 8) to ascertain the mass of uric acid molecules.

It is worth mentioning that equation (8) is a conventional equation mostly used to measure the mass by a cantilever^{45,46}.

$$\Delta m = \frac{k_N}{4\pi^2} \left(\frac{1}{f_N^2} - \frac{1}{(f_N - \Delta f_N)^2} \right) \quad (8)$$



The variation between the measured and the expected mass (calculated based on concentration) was delineated in Figure 8. Once again, our mathematical model provided a more precise estimation of mass, while the model derived from literature failed to accurately gauge the mass of uric acid molecules, resulting in an underestimated mass value. Here, we also found that the modified cantilever is capable of measuring the mass of uric acid molecules more accurately than the pristine cantilever and we also observed that the MoS_2 -coated PPP-NCH cantilever is capable of measuring the mass of uric acid more precisely and accurately than the MoS_2 -coated TAP300DLC cantilever.

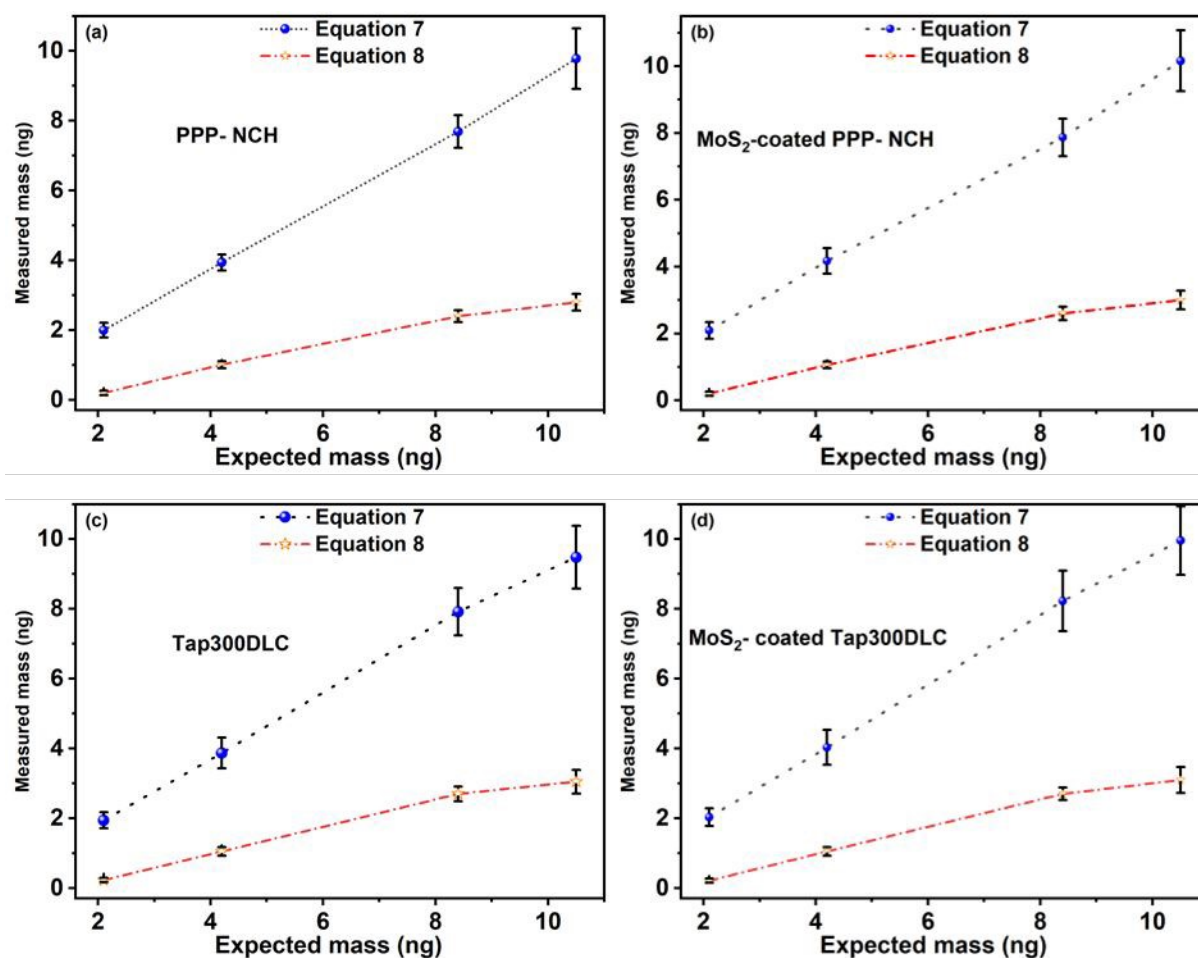


Fig. 8 Variation of expected mass (calculated from concentration) and measured mass calculated from (a) PPP-NCH cantilever (b) MoS_2 -coated PPP-NCH cantilever, (c) TAP300DLC cantilever and (d) MoS_2 -coated TAP300DLC cantilever using two different mathematical equations for Uric acid.

Conclusion

In summary, we have employed a theoretical and simulative model to analyze the effect of the coating layer on the frequency response of cantilevers. Subsequently, we presented a deposition methodology to coat the cantilever surface with 2D materials via the Van der Waals Epitaxy (VdWE) approach. We demonstrate the capability of our developed methodology to measure the mass, thickness, number of layers and Young's modulus of 2D materials. Furthermore,



following the digital twin concept, our proposed approach can precisely control the characteristics of 2D materials coated microcantilever and benefit from the exotic properties of 2D materials for sensing applications requiring highly sensitive detection characteristics. We demonstrate that the developed MoS₂-coated cantilever has higher responsivity than the pristine counterpart, which offers higher accuracy in mass spectrometry measurements.

Materials and Methods

AFM Probe

We employ the Asylum Research Oxford Jupiter AFM system to assess the natural frequencies and the spring constants of all the cantilevers in ambient conditions. The specific cantilevers utilized for our experimental measurement are (a) SCM-PIC (Nanoworld, Switzerland) with nominal dimensions: length: 450 μm , width: 50 μm , and thickness: 2.5 μm (b) PPP-NCH (Nanosensors Switzerland) with nominal dimensions: length: 125 μm , width: 30 μm and thickness: 4 μm and (c) TAP300DLC (Budget Sensor, Bulgaria) with nominal dimensions: length: 125 μm , width: 30 μm and thickness: 4 μm .

Deposition of MoS₂ on cantilevers

The MoS₂ 2D layers were fabricated on a Si wafer with a 300 nm SiO₂ layer (300 nm SiO₂/Si) or a c-plane sapphire substrate by Van der Waals Epitaxy (VdWE)^{26,27,36,47}. The VdWE-grown few-layer MoS₂ on 300 nm SiO₂/Si substrate was spin-coated with 7% polystyrene (PS, Sigma-Aldrich) in toluene at the speed of 1000 rpm for 50 s, and then baked on a hot plate at 90 °C for 15 min. The coated sample was subsequently attached to a supporting frame made with thermal release (TR) tape (from Nitto). Then the TR frame/PS/MoS₂/300 nm SiO₂/Si was immersed in the DI water to allow water to penetrate through the Van der Waals gap between MoS₂ and the 300 nm SiO₂/Si substrate. After that, the TR frame/PS/MoS₂ floated on the DI water and then further rinsed with DI water. The TR frame/PS/MoS₂ was ready for transfer on cantilevers, and then the TR frame was released by baking at 110°C for 30 mins. Finally, the PS layer was removed by immersing it in chloroform.

Characterization

The High-Resolution Transmission Electron Microscope (HRTEM) images were obtained by a JEOL 3010 Transmission electron microscope. The Raman spectra were acquired employing



a Renishaw inVia Raman spectrometer, utilizing a 532 nm laser, with an exposure time of 30 seconds and a laser power of 25 mW. X-ray photoelectron spectroscopy (XPS) was carried out by using a Thermo Scientific Theta Probe XPS System. The thermal noise data obtained from both cantilevers was employed for the determination of the individual eigenmodes of the cantilevers. The Scanning Electron Microscope images of the PPP-NCH cantilever were captured by a Hitachi SU5000 field-emission scanning electron microscope (FESEM).

View Article Online
DOI: 10.1039/D5NR03147H

Bacterial growth

Isolation, identification of an antibiotic-resistant (ARB) *E. coli*

E. coli was isolated from effluent samples collected at Carrickfergus Wastewater Treatment Works, Belfast, UK. The effluent was plated on selective Chromocult coliform agar, using membrane filtration following ISO 9308-1. The antibiotic resistance (ABR) of *E. coli* was tested against Trimethoprim (TMP), Sulfamethoxazole (SMX), Ofloxacin (OFX), Ampicillin (AMP), Tetracycline (TET) and Ciprofloxacin (CIP) to the minimum inhibitory concentration stated by the European Committee on Antimicrobial Susceptibility Testing (EUCAST) and Clinical Laboratory Standards Institute (CLSI). The standard protocol for freezing bacteria using glycerol (15%) and cryobeads was employed to maintain viable ARB *E. coli* stock in sterile tubes for further tests.

Microbially culture and analysis

A stock plate of the ABR *E. coli* was prepared using the frozen strains of ABR *E. coli*. The sample was taken from a freezer and a fresh culture was prepared using tryptic soy broth (TSB) inoculated with 2 single cryobeads and incubated at 37 °C for 21 h under constant agitation of 120 rpm in an orbital rotary shaker. An inoculation loop was then used to streak plate the *E. coli* from the TBS broth onto Chromocult coliform agar and stored at 4 °C in a fridge. A new stock was prepared each month to keep similar experimental conditions on the bacterial testing.

Culture and Suspending *E. coli* on PBS

E. coli was grown in TSB inoculated with 2 colonies from a stock plate using an inoculated loop and incubated at 37 °C for ~21 h under constant agitation of 120 rpm in an orbital rotary shaker overnight so that the bacteria were at the stationary growth phase. The bacterial broth was then centrifuged at 4000 rpm for 1 min to form a pellet. After the supernatant was removed, the pellet was resuspended in 10 ml of phosphate-buffered saline (PBS). The original sample



($\sim 10^8$ CFU/ml) was then diluted via serial 10-fold dilutions (twice) with PBS to a concentration of $\sim 10^6$ CFU/ml.

Enumeration of microorganisms

Serial dilutions (10-fold) were performed using PBS. Six drops of 10 μ L were plated on tryptic soy agar (TSA) this was done for each dilution and incubated at 37 $^{\circ}$ C for > 18 h. After which the plate dilution with a suitable number of countable colonies was enumerated and the average and associated deviation was calculated for a 5 μ l sample.

Uric Acid Solution

Uric acid and PBS tablets of analytical reagent (AR) grade were purchased from Sigma-Aldrich (UK) and were utilized without further purification. A 0.1 M PBS solution was prepared by dissolving the PBS tablets in ultrapure deionized (DI) water obtained from the Millipore Milli-Q system, with an electrical resistivity of 18 M Ω . A stock solution of 50 μ M uric acid was prepared and subsequently diluted using the PBS buffer to attain the desired concentration.

Simulations

In our simulation using MATLAB software, we have considered that the different layers of the 2D materials are deposited on our pristine cantilever. For the sake of our calculation, in this present study, we have utilized three different commercial cantilevers, (a) SCM-PIC (b) FMV-A and (c) QUEST R 200. The dimensions of the cantilevers are (a) SCM- PIC: length 450 μ m, width 50 μ m and thickness 2.5 μ m and (b) FMV-A: length 225 μ m, width 30 μ m and thickness 2.5 μ m and (c) QUEST R 200: length 200 μ m, width 30 μ m and thickness 0.9 μ m. The spring constants of both the cantilevers are 0.2 N/m 1.75 N/m and 0.2 N/m, respectively.

In the simulation work, we have considered 6 different 2D materials, which are (1) Molybdenum diselenide (MoSe₂), (2) Tungsten disulphide (WS₂), (3) Tungsten diselenide (WSe₂), (4) Titanium disulfide (TiS₂). (5) Graphene, and (6) Hexagonal boron nitride (hBN). The interlayer spacing, density and Young’s modulus of all the above-mentioned 2D materials are tabulated in Table 1.

Sample	Interlayer spacing (nm) ^{48,4950}	Density (kg/m ³) ^{51–53}	Young’s modulus (N/m ²) ^{54–58}
MoSe ₂	0.646	6900	154
WS ₂	0.618	7500	302



WSe ₂	0.651	8660	167	View Article Online DOI: 10.1039/D5NR03147H
TiS ₂	0.569	3220	228	
hBN	0.335	2100	866	
Graphene	0.335	2267	1000	

Acknowledgement

This work was supported by the Department for the Economy (DfE), Northern Ireland through US-Ireland R&D partnership grant No. USI 186, and the Engineering and Physical Sciences Research Council (EPSRC) grants EP/N00762X/1, EP/V040030/1, and EP/Y003551/1. The authors would like to thank Dr. He Wang for the XPS measurement and Dr Shunca Wang for the TEM measurement.

References

1. Payam, A. F. & Passian, A. Imaging beyond the surface region: Probing hidden materials via atomic force microscopy. *Sci Adv* **9**, 1–19 (2023).
2. Sharif Azadeh, S. *et al.* Microcantilever-integrated photonic circuits for broadband laser beam scanning. *Nat Commun* **14**, (2023).
3. Glia, A., Deliorman, M. & Qasaimeh, M. A. 3D Generation of Multipurpose Atomic Force Microscopy Tips. *Advanced Science* **9**, 1–15 (2022).
4. Liu, T. *et al.* Ballistic dynamics of flexural thermal movements in a nanomembrane revealed with subatomic resolution. *Sci Adv* **8**, 1–5 (2022).
5. Tamayo, J., Kosaka, P. M., Ruz, J. J., Paulo, Á. S. & Calleja, M. Biosensors based on nanomechanical systems. *Chem Soc Rev* **42**, 1287–1311 (2013).
6. Arlett, J. L., Myers, E. B. & Roukes, M. L. Comparative advantages of mechanical biosensors. *Nat Nanotechnol* **6**, 203–215 (2011).
7. Gupta, A. K. *et al.* Anomalous resonance in a nanomechanical biosensor. *Proc Natl Acad Sci U S A* **103**, 13362–13367 (2006).
8. Zhao, Y. *et al.* Achieving Ultrasensitivity and Long-Term Durability Simultaneously for Microcantilevers Inspired by a Scorpion's Circular Tip Slits. *ACS Nano* **16**, 18048–18057 (2022).
9. Incaviglia, I. *et al.* Tailoring the Sensitivity of Microcantilevers To Monitor the Mass of Single Adherent Living Cells. *Nano Lett* **23**, 588–596 (2023).
10. Liu, Y., Tian, Y., Lin, C., Miao, J. & Yu, X. A monolithically integrated microcantilever biosensor based on partially depleted SOI CMOS technology. *Microsyst Nanoeng* **9**, (2023).
11. Hanay, M. S. *et al.* Inertial imaging with nanomechanical systems. *Nat Nanotechnol* **10**, 339–344 (2015).
12. Stassi, S. *et al.* Large-scale parallelization of nanomechanical mass spectrometry with weakly-coupled resonators. *Nat Commun* **10**, (2019).
13. Kosaka, P. M. *et al.* Detection of cancer biomarkers in serum using a hybrid mechanical and optoplasmonic nanosensor. *Nat Nanotechnol* **9**, 1047–1053 (2014).
14. Gil-Santos, E. *et al.* Nanomechanical mass sensing and stiffness spectrometry based on two-dimensional vibrations of resonant nanowires. *Nat Nanotechnol* **5**, 641–645 (2010).
15. Li, M., Tang, H. X. & Roukes, M. L. Ultra-sensitive NEMS-based cantilevers for sensing, scanned probe and very high-frequency applications. *Nat Nanotechnol* **2**, 114–120 (2007).
16. Yang, Y. T., Callegari, C., Feng, X. L., Ekin, K. L. & Roukes, M. L. Zeptogram-scale nanomechanical mass sensing. *Nano Lett* **6**, 583–586 (2006).
17. Hanay, M. S. *et al.* Single-protein nanomechanical mass spectrometry in real time. *Nat Nanotechnol* **7**, 602–608 (2012).
18. Sansa, M. *et al.* Optomechanical mass spectrometry. *Nat Commun* **11**, 1–7 (2020).



19. Bhattacharya, G., Lionadi, I., Stevenson, A., Ward, J. & Payam, A. F. Tailored Microcantilever Optimization for Multifrequency Force Microscopy. *Advanced Science* **2303476**, 1–11 (2023).
20. Gorelkin, P. V. *et al.* Synthetic sialylglycopolymer receptor for virus detection using cantilever-based sensors. *Analyst* **140**, 6131–6137 (2015).
21. Wang, L. *et al.* Rapid and ultrasensitive electromechanical detection of ions, biomolecules and SARS-CoV-2 RNA in unamplified samples. *Nat Biomed Eng* **6**, 276–285 (2022).
22. Chaste, J. *et al.* A nanomechanical mass sensor with yoctogram resolution. *Nat Nanotechnol* **7**, 301–304 (2012).
23. Chiu, H. Y., Hung, P., Postma, H. W. C. & Bockrath, M. Atomic-scale mass sensing using carbon nanotube resonators. *Nano Lett* **8**, 4342–4346 (2008).
24. Pallandre, A., De Meersman, B., Blondeau, F., Nysten, B. & Jonas, A. M. Tuning the orientation of an antigen by adsorption onto nanostrapped templates. *J Am Chem Soc* **127**, 4320–4325 (2005).
25. Bhattacharya, G. *et al.* Mass and Stiffness Deconvolution in Nanomechanical Resonators for Precise Mass Measurement and In Vivo Biosensing. *ACS Nano* **18**, 20181–20190 (2024).
26. Felix, J. F. *et al.* A comprehensive study on the effects of gamma radiation on the physical properties of a two-dimensional WS₂ monolayer semiconductor. *Nanoscale Horiz* **5**, 259–267 (2020).
27. Huang, C. C. *et al.* Facilitating Uniform Large-Scale MoS₂, WS₂ Monolayers, and Their Heterostructures through van der Waals Epitaxy. *ACS Appl Mater Interfaces* **14**, 42365–42373 (2022).
28. Nan, Y., Tan, D., Shao, J., Willatzen, M. & Wang, Z. L. 2D Materials as Effective Cantilever Piezoelectric Nano Energy Harvesters. *ACS Energy Lett* **6**, 2313–2319 (2021).
29. Lee, J. *et al.* Electrically tunable single- and few-layer MoS₂ nanoelectromechanical systems with broad dynamic range. *Sci Adv* **4**, 27–35 (2018).
30. Aidi, B., Shaat, M., Abdelkefi, A. & Case, S. W. Free vibration analysis of cantilever open-hole composite plates. *Meccanica* **52**, 2819–2836 (2017).
31. Stephen, N. G. Beam vibration under compressive axial load-upper and lower bound approximation. *J Sound Vib* (1989).
32. Whiting, R., Angadi, M. A. & Tripathi, S. Evaluation of elastic moduli in thin-film/substrate systems by the two-layer vibrating reed method. *Materials Science and Engineering B* **30**, 35–38 (1995).
33. Zgheib, E., Alhussein, A., Slim, M. F., Khalil, K. & François, M. Multilayered models for determining the Young's modulus of thin films by means of Impulse Excitation Technique. *Mechanics of Materials* **137**, 103143 (2019).
34. Cho, H., Park, Y. & Kouh, T. Combined effect of mass and stiffness on the dynamics of a double-layered microcantilever. *Applied Physics Express* **14**, (2021).
35. Farrokh Payam, A. & Fathipour, M. Study of the tip mass and interaction force effects on the frequency response and mode shapes of the AFM cantilever. *The International Journal of Advanced Manufacturing Technology* **65**, 957–966 (2013).
36. Orsi Gordo, V. *et al.* Revealing the nature of lower temperature photoluminescence peaks by laser treatment in van der Waals epitaxially grown WS₂ monolayers. *Nanoscale* **10**, 4807–4815 (2018).
37. Li, X. & Zhu, H. Two-dimensional MoS₂: Properties, preparation, and applications. *Journal of Materiomics* **1**, 33–44 (2015).
38. Yuan, P., Li, C., Xu, S., Liu, J. & Wang, X. Interfacial thermal conductance between few to tens of layered-MoS₂ and c-Si: Effect of MoS₂ thickness. *Acta Mater* **122**, 152–165 (2017).
39. Ye, M., Winslow, D., Zhang, D., Pandey, R. & Yap, Y. K. Recent advancement on the optical properties of two-dimensional molybdenum disulfide (MoS₂) thin films. *Photonics* **2**, 288–307 (2015).



40. Castellanos-Gomez, A., Poot, M., Steele, G. A., Zant, H. S. J. van der & Nicolás Agraït, and G. R.-B. Elastic Properties of Freely Suspended MoS₂ Nanosheets. *Advanced Materials* **24**, 772–775 (2012). View Article Online
DOI:10.1039/D5NR03147H
41. Cafolla, C., Voïtchovsky, K. & Payam, A. F. Simultaneous quantification of Young's modulus and dispersion forces with nanoscale spatial resolution. *Nanotechnology* **34**, (2023).
42. Chang, J., Toga, K. B., Paulsen, J. D., Menon, N. & Russell, T. P. Thickness Dependence of the Young's Modulus of Polymer Thin Films. *Macromolecules* **51**, 6764–6770 (2018).
43. Sader, J. E. *Frequency Response of Cantilever Beams Immersed in Viscous Fluids with Applications to the Atomic Force Microscope*. (1998).
44. Cafolla, C., Payam, A. F. & Voïtchovsky, K. A non-destructive method to calibrate the torsional spring constant of atomic force microscope cantilevers in viscous environments. *J Appl Phys* **124**, (2018).
45. Łabędź, B., Wańczyk, A. & Rajfur, Z. Precise mass determination of single cell with cantilever-based microbiosensor system. *PLoS One* **12**, 1–14 (2017).
46. Incaviglia, I. *et al.* Tailoring the Sensitivity of Microcantilevers To Monitor the Mass of Single Adherent Living Cells. *Nano Lett* **23**, 588–596 (2023).
47. Huang, Z. W. *et al.* Terahertz analysis of CH₃NH₃PbI₃ perovskites associated with graphene and silver nanowire electrodes. *ACS Appl Mater Interfaces* **13**, 9224–9231 (2021).
48. Hod, O. Graphite and hexagonal boron-nitride have the same interlayer distance. Why? *J Chem Theory Comput* **8**, 1360–1369 (2012).
49. Jun Xu, Junjun Zhang, Wenjun Zhang, and C.-S. L. Advanced Energy Materials - 2017 - Xu - Interlayer Nanoarchitectonics of Two-Dimensional Transition-Metal Dichalcogenides.pdf. *Advanced Energy Materials* vol. 7 1700571 Preprint at (2017).
50. Rasool, H. I., Ophus, C., Klug, W. S., Zettl, A. & Gimzewski, J. K. Measurement of the intrinsic strength of crystalline and polycrystalline graphene. *Nat Commun* **4**, (2013).
51. Torrisi, L., Cutroneo, M., Torrisi, A. & Silipigni, L. Measurements on Five Characterizing Properties of Graphene Oxide and Reduced Graphene Oxide Foils. *Physica Status Solidi (A) Applications and Materials Science* **219**, 1–9 (2022).
52. Du Frane, W. L., Cervantes, O., Ellsworth, G. F. & Kuntz, J. D. Consolidation of cubic and hexagonal boron nitride composites. *Diam Relat Mater* **62**, 30–41 (2016).
53. The Materials Project. <https://legacy.materialsproject.org/>.
54. Pereira Júnior, M. L. *et al.* On the elastic properties and fracture patterns of MoX₂ (X = S, Se, Te) membranes: A reactive molecular dynamics study. *Condens Matter* **5**, 1–11 (2020).
55. Falin, A. *et al.* Mechanical Properties of Atomically Thin Tungsten Dichalcogenides: WS₂, WSe₂, and WTe₂. *ACS Nano* **15**, 2600–2610 (2021).
56. Jiang, Y. *et al.* Advances in TiS₂ for energy storage, electronic devices, and catalysis: A review. *Progress in Natural Science: Materials International* **33**, 133–150 (2023).
57. Papageorgiou, D. G., Kinloch, I. A. & Young, R. J. Mechanical properties of graphene and graphene-based nanocomposites. *Prog Mater Sci* **90**, 75–127 (2017).
58. Falin, A. *et al.* Mechanical properties of atomically thin boron nitride and the role of interlayer interactions. *Nat Commun* **8**, 1–9 (2017).



The data supporting the findings of this study, including the theoretical models, simulation results, and experimental data presented are available at main manuscript and Supplementary Materials. Additional data, including raw frequency shift measurements, Young’s modulus estimations, and mass sensing results for bacterial and uric acid concentrations, have been included as part of the Supplementary Information. If additional data is required, we are happy to provide and add in Supplementary Information.

[View Article Online](#)
DOI: 10.1039/D5NR03147H

